Magnetic Resonance Imaging 63 (2019) 37–48

Contents lists available at ScienceDirect

Magnetic Resonance Imaging

journal homepage: www.elsevier.com/locate/mri

Original contribution

A divide-and-conquer approach to compressed sensing MRI

Liyan Sun[a], Zhiwen Fan[a], Xinghao Ding[a,*], Congbo Cai[b], Yue Huang[a], John Paisley[c]

[a] Fujian Key Laboratory of Sensing and Computing for Smart City, Xiamen University, China
[b] Department of Electronic Science, Xiamen University, Xiamen, China
[c] Department of Electrical Engineering, Columbia University, New York, NY, USA

ARTICLE INFO

Keywords:
Compressed sensing
Magnetic resonance imaging
Divide-and-conquer

ABSTRACT

Compressed sensing (CS) theory assures us that we can accurately reconstruct magnetic resonance images using fewer k-space measurements than the Nyquist sampling rate requires. In traditional CS-MRI inversion methods, the fact that the energy within the Fourier measurement domain is distributed non-uniformly is often neglected during reconstruction. As a result, more densely sampled low frequency information tends to dominate penalization schemes for reconstructing MRI at the expense of high frequency details. In this paper, we propose a new framework for CS-MRI inversion in which we decompose the observed k-space data into "subspaces" via sets of filters in a lossless way, and reconstruct the images in these various spaces individually using off-the-shelf algorithms. We then fuse the results to obtain the final reconstruction. In this way, we are able to focus reconstruction on frequency information within the entire k-space more equally, preserving both high and low frequency details. We demonstrate that the proposed framework is competitive with state-of-the-art methods in CS-MRI in terms of quantitative performance, and often improves an algorithm's results qualitatively compared with its direct application to k-space.

1. Introduction

MRI is an important medical imaging technique because of its harmlessness and the high resolution information it measures in soft tissue. The data acquisition process directly measures Fourier coefficients of the object being imaged, which can then be recovered by an inverse Fourier transformation. A significant drawback of MR imaging is that data acquisition is relatively slow, meaning that a patient has to remain still for a long time to avoid producing motion artifacts. This is something especially difficult for children and those who are critically ill. Thus, accelerating the measurement speed while maintaining a diagnostic-quality reconstruction is a major challenge in MR imaging.

Compressive sensing (CS) theory [1,2] has shown that it is possible to accurately reconstruct MR images with significantly fewer measurements than mandated by the Nyquist sampling theorem [3-5]. The typical approach to CS-MRI can be generalized as the optimization problem

$$x = \arg\min_x \frac{\mu}{2}\|F_u x - y\|_2^2 + \rho(x). \quad (1)$$

The goal is to reconstruct the vector $x \in \mathbb{C}^N$, which corresponds to values in the MR image $X \in \mathbb{C}^{\sqrt{N}\times\sqrt{N}}$. The matrix $F_u \in \mathbb{C}^{u\times N}, u < N$ is an undersampled Fourier basis used to directly measure the k-space data $y \in \mathbb{C}^u$. In this objective, the first term enforces that the Fourier coefficients of x agree with the observations y. Since many vectors x will satisfy this requirement, the penalty $\rho(x)$ regularizes x with additional desired properties such as smoothness with the regularization parameter μ.

Different sparse bases include wavelets [6], total variation [6-8], and contourlets [9] are leveraged as regularizators in the framework of Eq. (1). Patch-based bases include directional wavelets (PBDWS) [10,11], a graph-based redundant wavelet transform (GBRWT) [12], and dictionary bases constructed *in situ* using dictionary learning algorithms like KSVD [13] and BPFA [14].

Some particular methods that we highlight and will use are the patch-based directional wavelet (PBDWS) [10,11], fast composite split algorithm (FCSA) and wavelet-tree based MRI (WatMRI) [15]. This CS-MRI objective function in PBDWS assumes that patches extracted and vectorized from the reconstructed MRI are sparse in the Haar wavelet domain. A key novelty is that each patch is vectorized in a way that depends on the geometric structure of the signal in that patch, and is chosen such that sparsity is maximized. In this way, image details can be preserved better while satisfying the need for sparsity. Regular wavelet and total variation regularization terms are combined to constrain the ill-posed problem in FCSA [16], where a highly efficient optimization was presented. A tree-structure wavelet representation was used to replace the regular wavelet term in WatMRI [17,15].

* Corresponding author.
E-mail address: dxh@xmu.edu.cn (X. Ding).

https://doi.org/10.1016/j.mri.2019.06.014
Received 21 December 2018; Received in revised form 19 June 2019; Accepted 22 June 2019

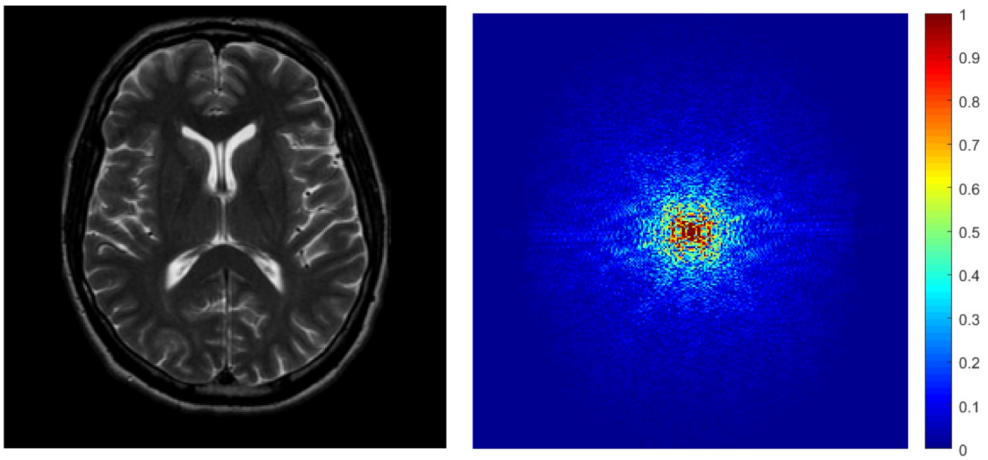

(a) Brain MRI (b) k-space coefficients

Fig. 1. k-space corresponding to a brain MRI.

Although impressive reconstruction qualities have been achieved in the previous researches, a key observation has been overlooked: k-space data is known to be distributed non-uniformly in energy, as illustrated with the brain MRI in Fig. 1. While k-space magnitudes tend to be larger in low frequency bands, much diagnostically important detail information is known to be in the high frequency regions. However, many existing CS-MRI methods treat all errors equally with the regular data fidelity term $\|F_u x - y\|_2^2$. From the perspective of maximum a posterior (MAP) in Bayesian theory [18], such a ℓ_2 term assumes every entry in the error vector $F_u x - y$ follows the Gaussian distribution with identical variance, imposing the absolute errors on the whole k-space on the same range. Suffering the errors of the same range as the low frequency ones, high frequency components containing fine details are more influenced because of their small magnitudes.

To further analyze the phenomenon, we define the following two simple measures: the *k-space absolute reconstruction error* (KARE) and the *k-space relative reconstruction error* (KRRE). These are the same size as the k-space, with the $(i,j)^{th}$ element denoted as follows,

$$(\mathrm{KARE})_{ij} = |(Y_r)_{ij} - (Y_f)_{ij}| \tag{2}$$

$$(\mathrm{KRRE})_{ij} = |(Y_r)_{ij} - (Y_f)_{ij}|/|(Y_f)_{ij}|. \tag{3}$$

Here, $Y_f \in \mathbb{C}^{\sqrt{N}\times\sqrt{N}}$ is the fully-sampled k-space data, and $Y_r \in \mathbb{C}^{\sqrt{N}\times\sqrt{N}}$ is the k-space of the MRI reconstructed from subsamples.

For the same brain MRI, we plot in Fig. 2 the reconstructed image and the corresponding KARE and KRRE images using a CS-MRI inversion method called PBDWS [11] with 10% under-sampling and a 2D random mask. In Fig. 2 (a) and (b), we observe that data in the peripheral high frequency regions suffer almost the same absolute but larger relative errors, which proves our claim on the k-space error distribution. As an illustrative experiment under the assumption that we have access to the fully-sampled k-space, one can manually redistribute the k-space error from PBDWS to move the errors from high frequency regions to low frequency ones to even the relative errors in whole k-space in such a way that the PSNR remains unchanged, as shown in Fig. 2 (c) and d. However, as shown in Fig. 2 (e) and (f), after redistribution the reconstruction has much better visual quality, and a larger structural similarity measure (SSIM). The PSNR stays the same during the error redistribution, proving the improvement in visual quality is not resulted from a boost in PSNR index, but the advance in reconstruction accuracy in high frequency bands.

This simulation proves the importance of further preserving high frequency k-space information even though low and high frequency components are reconstructed equally accurately. In some previous works, such information is implicitly modeled, however, to our knowledge this problem has not been explicitly addressed for CS-MRI inversion problems.

For example, in Ref. [19] , the low frequency k-space data is reconstructed first because of its dense distribution, then the reconstructed low frequency portions are padded back to the measurements for the second-stage reconstruction. The performance improvement of this method is limited due to fact that the reconstruction error of the low frequency bands propagate to the later reconstruction. The high and low frequency regions are separated using the rectangle box which can cause Gibbs effects and introduce artifacts. In Refs.[7,8], the horizontal and vertical differential images are reconstructed and then used as gradient constraints, where they mainly focus on the sparse nature of MRI in the gradient domain. In Ref. [20], a convolutional constraint is proposed, but the work lacks the discussion on non-uniformity in k-space. In Ref. [21], a method called HiSub CS-MRI formalized a link between the k-space and wavelet domain to apply separate under-sampling and reconstruction for high/low frequency k-space data. In the HiSub method, the high/low frequency regions in k-space are defined based on the separation of wavelet subbands; compressed sensing techniques are used for the high frequency region while parallel imaging is used for the low frequency region. The HiSub method relies on the specific sampling pattern and is not exclusively based on CS-MRI ideas. In Ref. [22], the local scale mixture model is proposed to decompose the MR images into dual block sparse components: total variation for piecewise smooth parts and wavelet for residuals, but the decomposition only depends on the different priors between the total variation and wavelet in spatial domain. All the above works proved the benefits of separate high and low frequency information for reconstruction, although the insight that high frequency information should be better preserved with respect to the relative reconstruction error lacks. As we observed the magnitudes of high and low frequency bands in k-space differ significantly, decouple the weaker signals from the stronger ones is a reasonable approach to high frequency information protection.

The above analysis motivates us to reconsider the CS-MRI problem using a divide-and-conquer (DAC) framework that can be implemented using existing inversion algorithms. Our method consists of three steps: subspace decomposition, subspace reconstruction and subspace integration. While the word “subspace” is well-defined for linear algebra, here we mean a specific frequency view into which the k-space measurements are decomposed using standard filtering techniques. This method allows for the algorithms to deal with the high and low frequency k-space data separately to better preserve fine structural details. Although the idea is simple, we note that the proposed subspace method exhibits great potential for recovering fine details in MRI by better preserving the high frequency information possibly improving

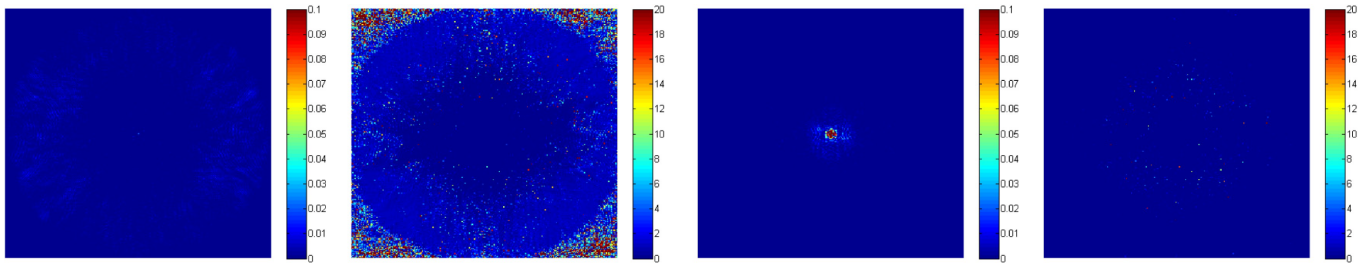

(a) KARE map of PBDWS (b) KRRE map of PBDWS (c) Redistributed KARE (d) Redistributed KRRE

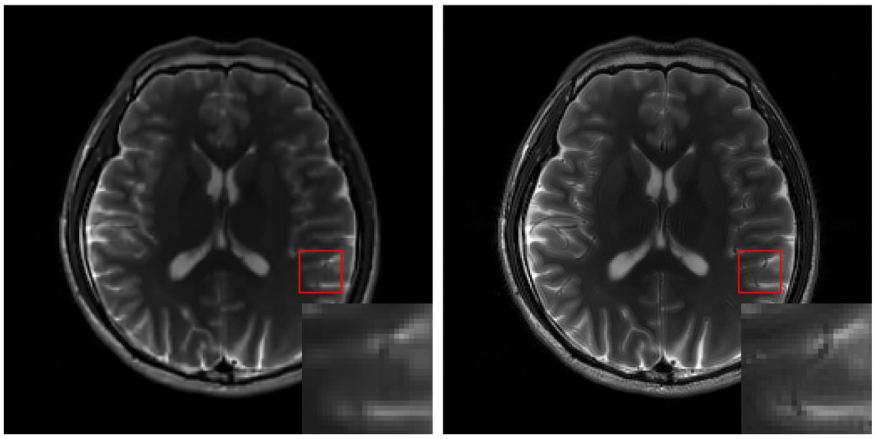

(e) PBDWS (SSIM = 0.91) (f) Redistributed (SSIM = 0.97)

Fig. 2. CS-MRI reconstruction results using PBDWS and an ad-hoc error redistribution for 10% 2D random sampling. Since the ground truth is not known in real experiments, this motivating example is purely illustrative. (a) The KARE map of the PBDWS reconstruction. (b) The KRRE map of the PBDWS reconstruction. (c) The KARE map of the redistributed k-space error reconstruction. (d) The KRRE map of the redistributed k-space error reconstruction. (e) CS-MRI reconstruction image using PBDWS. (f) CS-MRI reconstruction after error redistribution.

the diagnosis quality of medical imaging applications.[1]

2. Method

The proposed subspace method includes three steps: subspace decomposition, subspace reconstruction and subspace integration. We display a flowchart of the method in Fig. 3. In this section, we first discuss each of the three steps above separately. Then, we connect these three steps to the objective function given in Eq. (1). At the end of the section, we summarize the proposed DAC CS-MRI framework in Algorithm 1. Here, we adopt the HoriVert subspace decomposition for illustration, which we will elaborate in later section.

2.1. Subspace decomposition

In order to reconstruct the corresponding image in each subspace, we need to first define the subspaces and then obtain the partially observed k-space data in each subspace. We call this process subspace decomposition. According to signal processing theory [23], a lossless decomposition can be accomplished using filter bank if the frequency responses of the filters cover the whole frequency domain. In our case, we use a set of linear filters for their simplicity. We let $\{H_i\}_{i=1}^S$ be the impulse responses of the set of chosen filters, where S is selected in advance. In principle, a decomposition in the image domain can be formulated as follows,

$$X_{f_i} = X_f * H_i, \tag{4}$$

where $X_{f_i} \in \mathbb{C}^{\sqrt{N}\times\sqrt{N}}$ is the convolved image of the fully-sampled in the ith subspace and * denotes the 2D convolution. Eq. (4) is equivalent to

$$Y_{f_i} = Y_f \odot \widehat{H}_i, \tag{5}$$

where $Y_{f_i} \in \mathbb{C}^{\sqrt{N}\times\sqrt{N}}$ and $\{\widehat{H}_i \in \mathbb{C}^{\sqrt{N}\times\sqrt{N}}\}_{i=1}^S$ is the Fourier transformation of and H_i. The operation $\odot$ denotes element-wise multiplication.

It is straightforward to demonstrate the zero-filled under-sampled k-space data Y_i in each subspace can now be denoted as

$$Y_i = Y \odot \widehat{H}_i. \tag{6}$$

Eq. (6) shows that the partial k-space data decomposed in each subspace can be derived via the element-wise multiplication between the frequency response of the filter and the original partially observed k-space data Y. We will use this latter observation in our reconstruction algorithm.

The vectorized form of Eq. (4) can now be written as

$$x_{f_i} = \tilde{H}_i x_f, \tag{7}$$

where $x_{f_i} \in \mathbb{C}^N$ is the vectorized form of and $\{\tilde{H}_i \in \mathbb{R}^{N\times N}\}_{i=1}^S$ is a circulant matrix. Similarly, such vectorization can be applied to other formulations above. We next return to the filter banks considered in Section 2.4.

2.2. Subspace reconstruction

After dividing k-space into partial frequency views y_i, it is intuitive to exploit this isolated information and reconstruct the corresponding images in each subspace separately. This will ensure that high frequency information, captured in certain y_i by appropriate filter banks, is not sacrificed in favor of the far greater number of high magnitude, low frequency measurements. To this end, we define a subspace-specific

[1] We wish to emphasize here that our proposed method does *not* simply partition the k-space data into disjoint frequency regions.

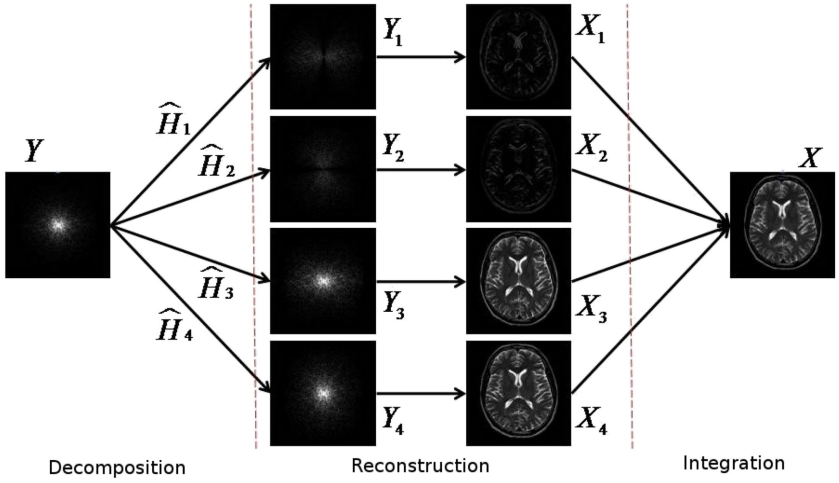

Fig. 3. Flowchart of proposed subspace method. A filter bank is applied on the original partial k-space data to acquire the subspace k-space measurements. Standard compressed sensing methods are leveraged to reconstructed each subspace. Then subspace images are fused to produce final estimation.

optimization problem with an appropriate regularization term to be determined. The reconstruction of each subspace can be formulated by minimizing the following objective function

$$\underset{x_i}{\operatorname{argmin}} \frac{\mu_i}{2} \|F_u x_i - y_i\|_2^2 + \rho_i(x_i), \tag{8}$$

where $\rho_i(x_i)$ enforces desired properties of the reconstructed subspace image and μ_i is the regularization parameter for the data fidelity term. As with the filters, H_i, these penalty functions ρ_i can be chosen to be any CS-MRI inversion algorithm. We note the new data fidelity squared error is proposed for better preservation for high frequency information, which also distinguish the proposed subspace method with merely regularizing the filtered subspace images with a unified data fidelity term. In this paper, we use three recent state-of-the-art CS-MRI reconstruction methods: FCSA [16], WatMRI [15] and PBDWS [10]. To summarize, these penalties are the following:

$$\rho_i(x_i) = \begin{cases} \alpha \mathrm{TV}(x_i) + \beta \|\Phi x_i\|_1 & \text{FCSA} \\ \alpha \mathrm{TV}(x_i) + \beta \|\Phi x_i\|_{\text{tree}} & \text{WatMRI} \\ \|B_w x_i\|_0 & \text{PBDWS} \end{cases} \tag{9}$$

We experiment with these three methods to show that our method can provide general improvement to many existing CS-MRI models. In our experiments, we apply the same reconstruction algorithm to all subspaces, but with different parameter settings. If the MRI is divided into n subspaces via $\tilde{H}_1, \ldots, \tilde{H}_n$, then the chosen algorithm would be run independently n times, once for each subspace. Therefore, our framework increases computation time by a factor of n, but the independence of each optimization allows for a straightforward parallelization.

2.3. Subspace integration

Since the subspace decomposition is a linear decomposition using linear filters, if the decomposition is complementary but not redundant then integrating these results into a final reconstruction can be done by simply adding the images together,

$$x = \sum_{i=1}^{N} x_i. \tag{10}$$

We also consider a Tikhonov regularization method by formulating the integration according to the following objective function

$$x = \arg\min_x \sum_{i=1}^{n} \lambda_i \|x_i - \tilde{H}_i x\|_2^2. \tag{11}$$

This objective function admits a closed-form solution, but direct computation is infeasible because of the high dimensionality of $\tilde{H}_i$. However, by transferring the problem to the Fourier domain the reconstructed k-space is calculated element-wise followed by an inverse Fourier transform,

$$X = F^H \left(\sum_i \lambda_i \widehat{H}_i^H \odot \widehat{X}_i \right) / \left(\sum_i \lambda_i \|\widehat{H}_i\|_2^2 \right). \tag{12}$$

Here, the division is element-wise, as is the magnitude of $\widehat{H}_i$ in the denominator. We discuss a method for determining each λ_i below in Section 2.5.

2.4. Filter banks for dividing and conquering

We consider two kinds of filter banks in this paper: one based on the horizontal and vertical redundant filter bank (HoriVert), and another based on the Gaussian complementary filter bank (Gaussian).

2.4.1. HoriVert subspace decomposition

Because much of the high frequency details in MRI can be represented as vertical or horizontal edges, we consider a decomposition of k-space into horizontal/vertical high and low frequency subspaces. We adopt the following four filters for decomposition: $h_1 = [-0.5, 0.5]$ and $h_3 = [0.5, 0.5]$ for vertical high and low frequency subspaces, and $h_2 = [-0.5, 0.5]^T$ and $h_4 = [0.5, 0.5]^T$ for horizontal high and low frequency subspace. The frequency responses of these filters satisfy the relationships

$$\widehat{H}_1 + \widehat{H}_3 = \mathbf{1} \tag{13}$$

$$\widehat{H}_2 + \widehat{H}_4 = \mathbf{1} \tag{14}$$

where $\mathbf{1}$ is the all-ones matrix. It's easy to verify that

$$Y_1 + Y_3 = Y \odot H_1 + Y \odot H_3 = Y(H_1 + H_3) = Y \tag{15}$$

$$Y_2 + Y_4 = Y \odot H_2 + Y \odot H_4 = Y(H_2 + H_4) = Y \tag{16}$$

Therefore, the proposed filtering scheme is redundant and meets the requirements for completeness, and is thus lossless. We call this proposed decomposition scheme the HoriVert subspace decomposition. We display the frequency responses of these filter banks in Fig. 4 (a)–(d).

2.4.2. Gaussian subspace decomposition

We also test our DAC method using spatial Gaussian filters. We design the Gaussian low-pass filter, denoted as g_{lp}, with 5×5 spatial support and unit standard deviation and similar for the corresponding high-pass filter, denoted g_{hp}. This gives frequency responses $\hat{G}_{lp}$ for g_{lp}

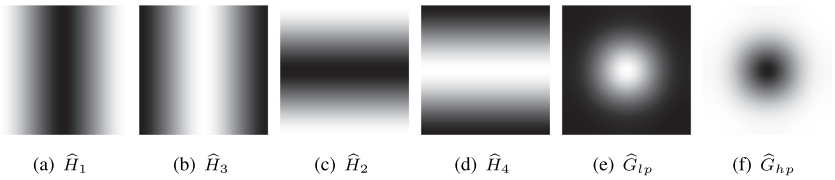

(a) $\widehat{H}_1$ (b) $\widehat{H}_3$ (c) $\widehat{H}_2$ (d) $\widehat{H}_4$ (e) $\widehat{G}_{lp}$ (f) $\widehat{G}_{hp}$

Fig. 4. The frequency response of the HoriVert redundant filter banks and the Gaussian complementary filter banks. White corresponds to one and black corresponds to zero, with a smooth transition in between. (a)–(f) are respectively the vertical high frequency, vertical low frequency, horizontal high frequency, horizontal low frequency, Gaussian low frequency, and Gaussian high frequency filters.

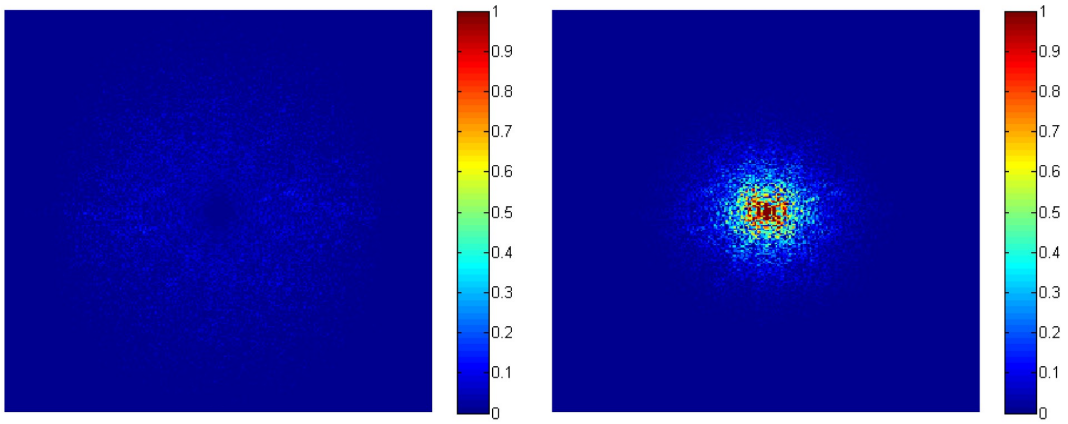

(a) high frequency subspace (b) low frequency subspace

Fig. 5. The high and low frequency subspaces of a brain MRI obtained with the Gaussian filtering decomposition corresponding to Fig. 4 (e) and f. The sum of Fig. 5 (a) and (b) is equal to Fig. 1b. However, we note that these are not simply disjoint partitions of the space.

and $\hat{G}_{hp}$ for g_{hp}. $\hat{G}_{lp}$ and $\hat{G}_{hp}$ have a similar lossless property,

$$\widehat{G}_{lp} + \widehat{G}_{hp} = \mathbf{1}. \tag{17}$$

We also show the frequency response of the Gaussian complementary filter banks in Fig. 4 (e) and (f).

To illustrate the proposed decomposition scheme, we show the brain MRI k-space magnitudes of the two subspaces using Gaussian subspace decomposition scheme in Fig. 5. The sum of Fig. 5 (a) and (b) is equal to Fig. 1 (b). However, as Fig. 5(a) and (b) indicates, these subspaces do not simply correspond to disjoint partitions of k-space. Also in Fig. 5 (a), we observe the magnitudes within the high frequency subspace keep in the same range, which will benefit the k-space relative reconstruction accuracy.

To further analyze the benefit of applying reconstruction on high frequency subspace for detail protection, we give an MRI brain image and its wavelet coefficients in Fig. 6. We observe the low frequency

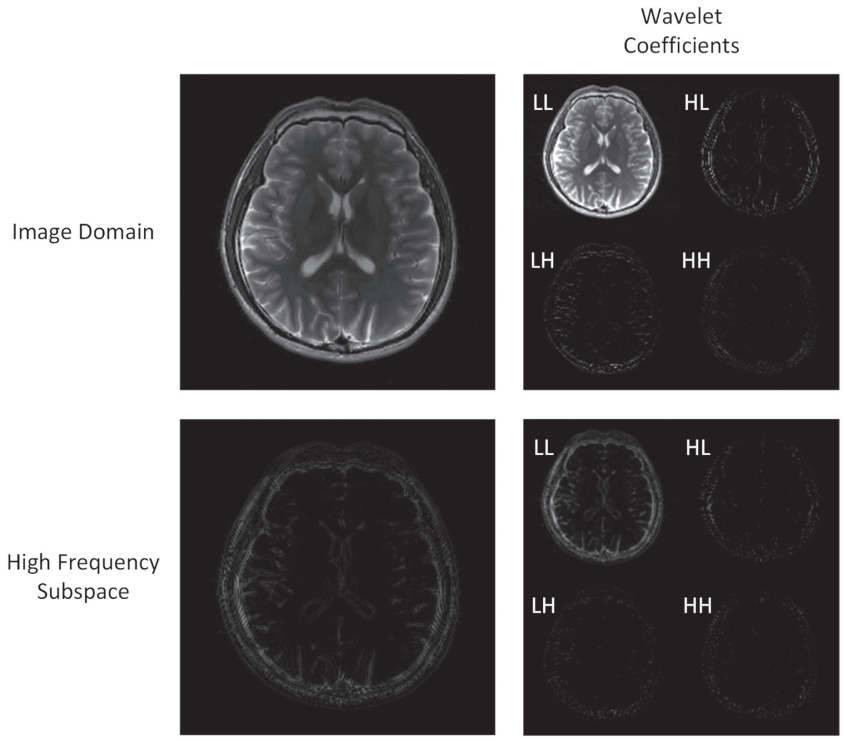

Fig. 6. We show the wavelet coefficients of a brain MRI and its high frequency subspace obtained via Gaussian subspace decomposition.

wavelet coefficients have much larger magnitudes. When thresholding algorithm is applied on the all wavelet bands with an identical threshold, the fine details in high frequency coefficients tend to be eliminated. Here, we also show the wavelet coefficients of the decomposed high frequency subspace obtained via Gaussian filter banks. We observe the wavelet coefficients are within the similar numeric range. Hence, the subspace reconstruction in high frequency subspace can help better preserve details when thresholding algorithm is applied.

2.5. An equivalent objective

We next briefly summarize the basic objective function that our DAC algorithm is optimizing. Recall that the typical objective function for CS-MRI has the form

$$x = \arg\min_x \frac{\mu}{2}\|y - F_u x\|_2^2 + \rho(x). \tag{18}$$

In the algorithm described above, we modify this to

$$x = \arg\min_x \sum_{i=1}^{n} \lambda_i \|H_i x - x_i\|_2^2 + \min_{x_i} \frac{\mu_i}{2}\|y_i - F_u x_i\|_2^2 + \rho_i(x_i). \tag{19}$$

As can be seen, we minimize in two parts. First, we minimize x_i over the two right-most terms in the "divide" portion of the algorithm. We then minimize over x in the first term using the learned x_i. This way, the low and high frequency subspaces can contribute more equally to the reconstruction of x.

Finally, the setting of λ_i is important when reconstructing the MRI x. We found that a uniform setting consistently works well. As another approach, viewing the first term as an augmented Lagrangian that attempts to enforce what is originally a strict equality $x_i = H_i x$, we also experiment with maximizing over λ_i in an adversarial manner to try and enforce these equalities (subject to $\|\lambda\|_2 = 1$). We use this approach in our experiments. We summarize the entire procedure in Algorithm 1.

Algorithm 1. Divide-and-conquer CS-MRI

Input sub-sampled k-space y and Fourier basis F_u.

Select subspace filters $H_1, \ldots, H_n$.

Select CS-MRI penalizations $\rho_1, \ldots, \rho_n$.

for each i **do**

  Filter y using the ith filter as in Equation (6).

  Optimize $x_i = \arg\min_{x_i} \frac{\mu_i}{2}\|y_i - F_u x_i\|_2^2 + \rho_i(x_i)$.

end for

while not converged **do**

  Set $x = \arg\min_x \sum_{i=1}^{n} \lambda_i \|H_i x - x_i\|_2^2$ using Eq. (11).

  Set $\lambda_i = \|H_i x - x_i\|_2^2$ and normalize to unit L2 length.

end while

return Vectorized reconstructed MRI x.

3. Results

3.1. Experimental setup

For our experiments, we adopted three sampling masks [14]: 1D Cartesian sampling with random phase encodes, 2D random sampling, and pseudo radial sampling shown in Fig. 7. We conducted the simulations on the phantom shown in Fig. 7 (d) and the MRI-acquired complex-valued brain images shown in Fig. 7 (e), (f) and (g). These images were normalized to have maximum magnitudes of 1.

The Gaussian and HoriVert subspace filtering methods were compared using the three state-of-the-art CS-MRI methods described in Section 2.2. As performance measures, we used the peak signal-to-noise ratio (PSNR), the structural similarity index (SSIM), and the high frequency error norm (HFEN) [13]. The standard PSNR is a function of the MSE, but as we previously indicated, the PSNR measure is not the optimal choice in assessing the quality of an MR image. Therefore we also used SSIM and HFEN. SSIM measures the structural similarity of two images and is more consistent with the evaluation system of the human eye. HFEN has been proposed to evaluate the reconstruction quality of high frequency portions of MRI. In HFEN, the Laplacian of Gaussian (LoG) filter is used to extract the high frequency information within the MRI. HFEN is measured by the l_2 norm of the extracted features between the fully-sampled image and the reconstructed image.

All the experiments were coded in Matlab (R2014a). Computations were implemented with an Intel Core i5 CPU at 3.20 GHz and 8 Gb memory, employing a 64-bit Windows 7 operating system. For FCSA, WatMRI and PBDWS, we used the source code available from the authors' homepage, but we made parameter adjustments obtain the best performances.

3.2. Illustrative experiment on phantom data

The real-valued phantom image of the size 256 × 256 is piecewise constant and contains various image structures [24]. The simulation phantom was created via Matlab implementation. To show the advantage of

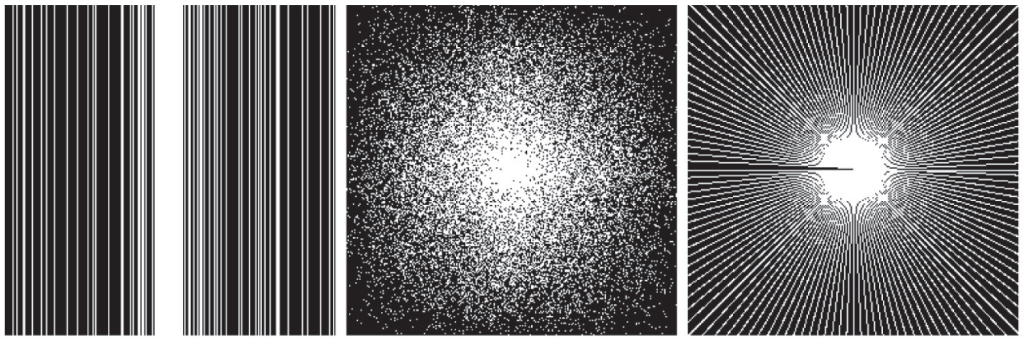

(a) 40% Cartesian mask (b) 30% random mask (c) 30% radial mask

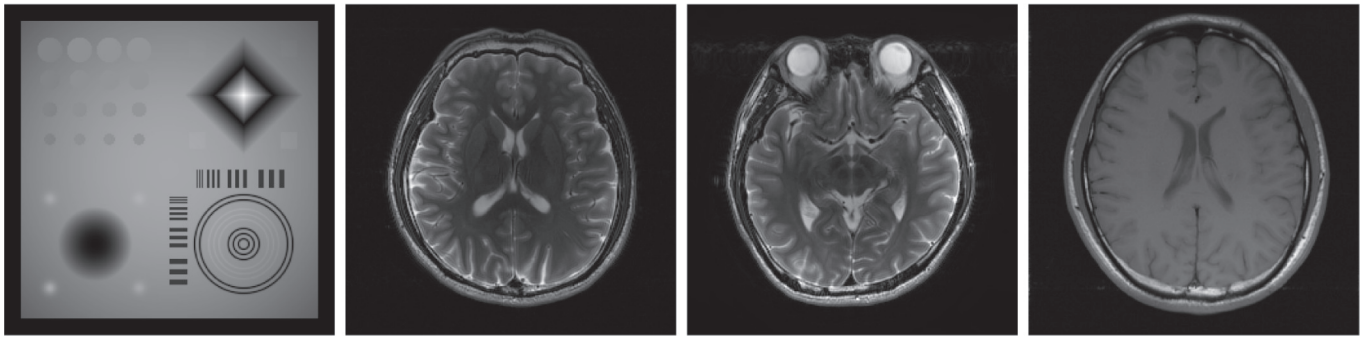

(d) phantom data (e) T2wBrain 27 th slice (f) T2wBrain 7 th slice (g) T1wBrain

Fig. 7. The MRI data and under-sampling masks used in our experiments.

our divide-and-conquer method, we compared the reconstruction result of the original PBDWS algorithm with HoriVert PBDWS with a 40% under-sampled Cartesian mask, 30% under-sampled random mask and 30% under-sampled radial mask. In Fig. 8, the phantom reconstructions and their corresponding error maps demonstrate that the proposed DAC method is able to reconstruct the high frequency data more accurately. Note that the same reconstruction algorithm was being used in both cases; the only difference was whether the sub-sampled k-space data was modeled directly or indirectly through different low and high pass filters.

3.3. Experiments on T2wBrain data

We also tested our DAC framework on a clinically-obtained brain MRI also experimented with in Refs. [9], [14], [25], [10] and [11]. In particular, we used the 7^{th} and 27^{th} slices (named in the acquisition order) of a complex-valued T2-weighted brain MRI (size 256×256) volume data called T2wBrain ("slice7" and "slice27" respectively, as shown in Fig. 7), which was 2D acquired with 32 coils from a healthy volunteer by a 3-T Siemens Trio Tim MRI scanner using the T2-weighted turbo spin echo sequence (TR/TE = 6100/99 ms, 220×220 mm^2 field of view, 3 mm slice thickness). We did SENSE reconstruction as the parallel imaging technique with reduction factor 1 to compose full k-space of gold standard images. The full k-space data will be used for emulate single-channel MRI.

We first tested the T2wBrain slice27 data using HoriVert PBDWS with different under-sampling patterns [2]. In Fig. 9, high frequency degradation is observable under different sampling masks in PBDWS reconstructions. With HoriVert PBDWS, these fine structures were recovered better. The corresponding error maps shown in Fig. 9 validate this observation. For further illustration, we plotted the KRRE maps of the reconstructions in Fig. 10. As can be seen, for our DAC method the high frequency regions of reconstructed k-space suffer less from errors than the direct method. This helps confirm our claim that isolating frequency content into subspaces for independent reconstruction allows for a more uniform reconstruction of k-space than the common squared error penalty.

The quantitative results for the 27^{th} slice of the T2wBrain data are given in Table 1. As is clear, CS-MRI methods like FCSA and PBDWS can be significantly improved using the proposed divide-and-conquer method. One interesting phenomenon is that, while the KRRE of Gaussian PBDWS is worse in high frequency regions than HoriVert PBDWS, the PSNR of Gaussian PBDWS is better than HoriVert PBDWS, while the SSIM and HFEN evaluation gives the opposite conclusion. This helps confirms the claim that the PSNR index does not provide a completely convincing measure of reconstruction quality in terms of detail recovery. SSIM and HFEN were designed to measure this, and these quantitative measures were more in agreement with the shown KRRE maps and subjective evaluation. Besides, we can observe the Gaussian FCSA failed to achieve better objective assessment index than its regular counterpart, however, the HoriVert FCSA worked well as expected. The phenomenon on the failing case may be attributed to the better robustness of the HoriVert framework over the Gaussian framework under ultra-low sampling ratios. The redundant subspace decomposition scheme of HoriVert DAC framework provided such robustness because multiple subspaces were combined to fuse the final estimation. At higher sampling ratios and other sampling patterns, both the Gaussian and HoriVert DAC frameworks provided stable improvements.

Finally, we also conducted experiments on the T2wBrain slice7 and slice27 using Gaussian and HoriVert FCSA and WatMRI using the 30% radial sampling pattern, as shown in Fig. 11 with error maps given. Again, Gaussian and HoriVert FCSA and WatMRI achieved better performance than their standard counterparts, manifesting the utility of the two subspace schemes.

[2] As mentioned, we set the parameters to their best experimentally-obtained values according to SSIM index. For PBDWS, we set the data fidelity parameter $\mu = 1e6$ for each subspace. We applied the same parameter setting for all the tested data. We detail the parameter setting in later Discussion section.

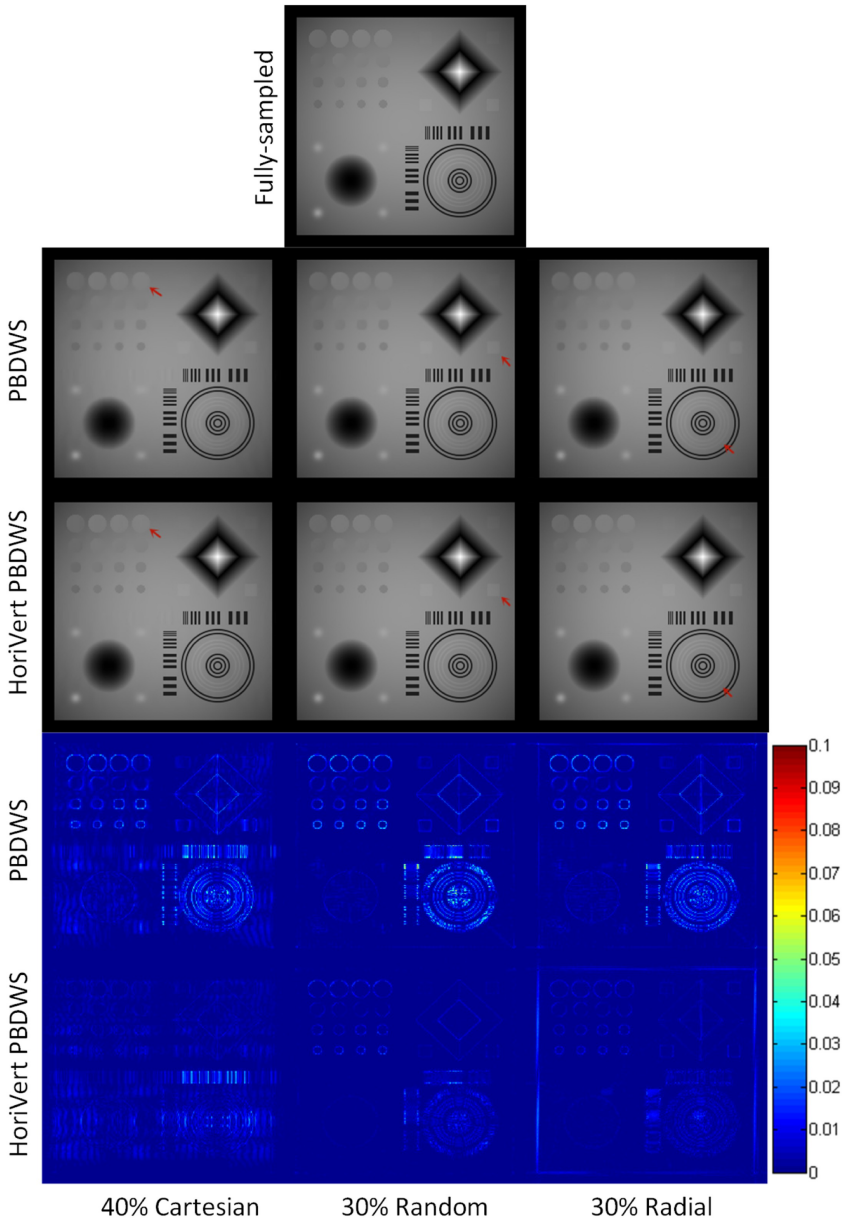

Fig. 8. The reconstruction errors results on phantom data using PBDWS and HoriVert PBDWS under three different under-sampling regimes.

3.4. Experiments on T1wBrain data

In addition to the complex-valued in-vivo T2-weighted brain MRI data, we also tested on a complex-valued in-vivo T1-weighted brain MRI image called T1wBrain to validate the proposed framework on different MRI modalities [15]. The T1wBrain image is an axial brain image from a 3 T commercial scanner (GE Healthcare, Waukesha, WI) with an eight-channel head coil (In Vivo, Gainesville, FL) using a two-dimensional T1-weighted spin echo protocol (TE/TR = 11/700 ms, 22 cm FOV, 10 slices, 256 × 256 matrix). We tested various CS-MRI algorithms on the T1wBrain data for comparison, including L1-ESPIRiT [26], pFISTA [27], PANO [25], PBDWS [11], GBRWT [12] and the proposed DAC Gaussian PBDWS. Note that L1-ESPIRiT used the parallel imaging technique, while we used a strategy similar to the T2wBrain data to emulate the single coil imaging for other algorithms. We have adjusted the parameters of these algorithms to their best performance in PSNR.

The reconstruction results and corresponding residual error images are shown in Figs. 12 and 13. The structural information was preserved better under the DAC Gaussian PBDWS compared with other CS-MRI methods. In Fig. 14, the Gaussian PBDWS achieved the highest PSNR and SSIM value meanwhile the lowest HFEN value.

For the Gaussian and HoriVert subspace methods, the computational time required is roughly two and four times greater than the corresponding regular methods because there are two and four corresponding optimizations, respectively, rather than one. This constituted the most computationally intensive part of the proposed DAC framework, but it is easily parallelizeable. For the subspace decomposition and subspace integration steps, the matrix Hadamard multiplication is computationally efficient.

4. Discussion

4.1. Discussion on parameter setting

In the proposed divide-and-conquer framework, parameters requiring tuning are in both the subspace reconstruction and subspace integration stages. If the chosen subspace reconstruction algorithm is robust to variations in parameter setting, such robustness can also benefit our DAC extension.

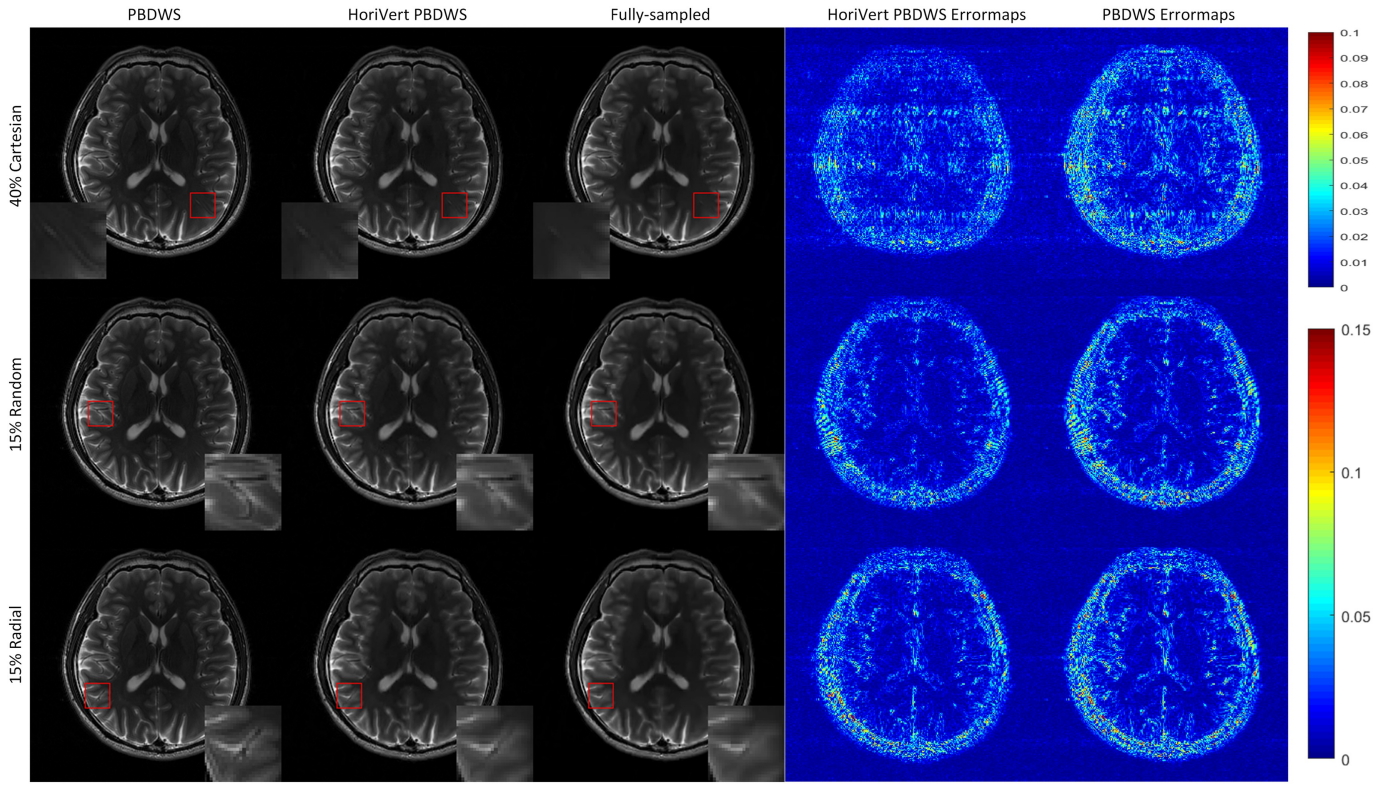

Fig. 9. The reconstruction results of PBDWS and HoriVert PBDWS on different sampling patterns and their corresponding error maps.

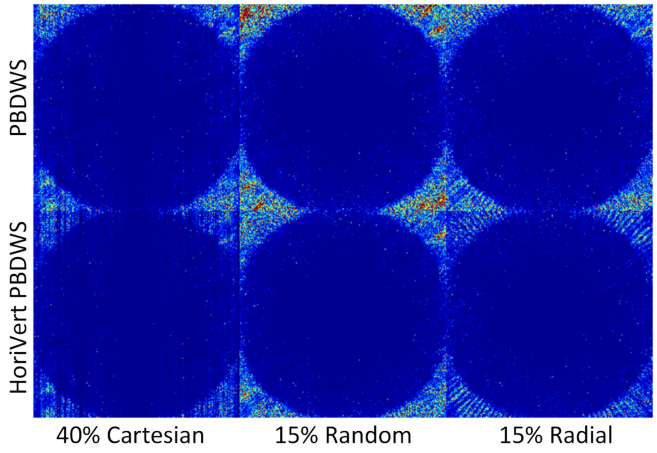

Fig. 10. The KRRE maps of the reconstructed images corresponds to the Fig. 9.

For subspace reconstruction using FCSA or WatMRI, the regularization parameters for both the TV and wavelet or tree wavelet terms can influence the subspace reconstruction because of the characteristics in high and low frequency k-space data. However, when we used no parameter tuning in the subspace reconstruction phase, the proposed method still outperformed the direct method by a considerable margin in Table 2. We conducted the experiment using FCSA on T2wBrain 27^{th} slice with 1D 40% mask. Here, we adopted the regularization parameter for TV term 0.002 and wavelet term 0.002, which has been proved achieving the best performance on the direct FCSA method. This proved the improvement of the proposed DAC framework is not simply a result of parameter tuning.

In the HoriVert and Gaussian PBDWS, the regularization parameter term on the data fidelity μ is a relative value between the data fidelity term and the other patch-based directional wavelet sparsity regularization term. On a certain subspace, the data fidelity term and sparsity regularization term both work on the same decomposed k-space data, so the relative value holds, leading to the data regularization para-

Table 1
PSNR|SSIM|HFEN of the reconstruction for the T2wBrain 27slice MRI using various sampling masks and rates. Larger values are better for PSNR and SSIM, smaller values for HFEN. In most cases, divide-and-conquer improved the base algorithm.

Mask	%	FCSA	Gauss FCSA	HoriVert FCSA	PBDWS	Gauss PBDWS	HoriVert PBDWS
Cartesian	25	28.70|0.850|1.476	28.45|0.850|1.559	28.93|0.869|1.452	34.12|0.924|0.824	34.52|0.944|0.833	34.44|0.950|0.741
	30	31.71|0.893|1.042	32.54|0.915|0.964	32.48|0.918|0.968	36.79|0.940|0.558	37.81|0.965|0.544	37.19|0.968|0.483
	35	32.16|0.903|0.944	33.08|0.926|0.888	33.06|0.929|0.884	37.58|0.945|0.511	38.67|0.971|0.487	38.18|0.973|0.435
	40	33.33|0.914|0.758	35.03|0.942|0.671	34.80|0.941|0.668	39.05|0.951|0.420	40.43|0.976|0.395	39.71|0.978|0.355
Random	15	31.04|0.896|0.676	32.20|0.922|0.608	32.39|0.927|0.596	34.72|0.933|0.462	35.94|0.960|0.390	35.37|0.961|0.365
	20	32.55|0.916|0.562	34.07|0.944|0.429	34.24|0.945|0.435	36.76|0.950|0.340	38.28|0.971|0.281	37.58|0.972|0.261
	25	33.22|0.926|0.530	35.23|0.952|0.360	35.19|0.950|0.385	38.03|0.951|0.291	40.01|0.978|0.226	39.06|0.979|0.215
	30	34.24|0.938|0.485	36.86|0.963|0.279	36.58|0.959|0.320	39.77|0.957|0.230	42.40|0.984|0.162	41.15|0.984|0.155
Radial	15	30.21|0.879|1.057	30.19|0.878|1.100	30.79|0.901|1.002	33.89|0.925|0.667	34.22|0.947|0.653	34.14|0.953|0.577
	20	31.90|0.906|0.775	32.29|0.908|0.742	32.92|0.925|0.678	35.91|0.940|0.492	36.88|0.965|0.440	36.47|0.968|0.399
	25	33.20|0.926|0.617	34.24|0.930|0.530	34.62|0.940|0.501	37.85|0.950|0.360	39.37|0.976|0.305	38.69|0.977|0.276
	30	34.09|0.935|0.546	35.75|0.943|0.413	35.77|0.947|0.424	39.24|0.955|0.290	41.42|0.981|0.233	40.36|0.982|0.212

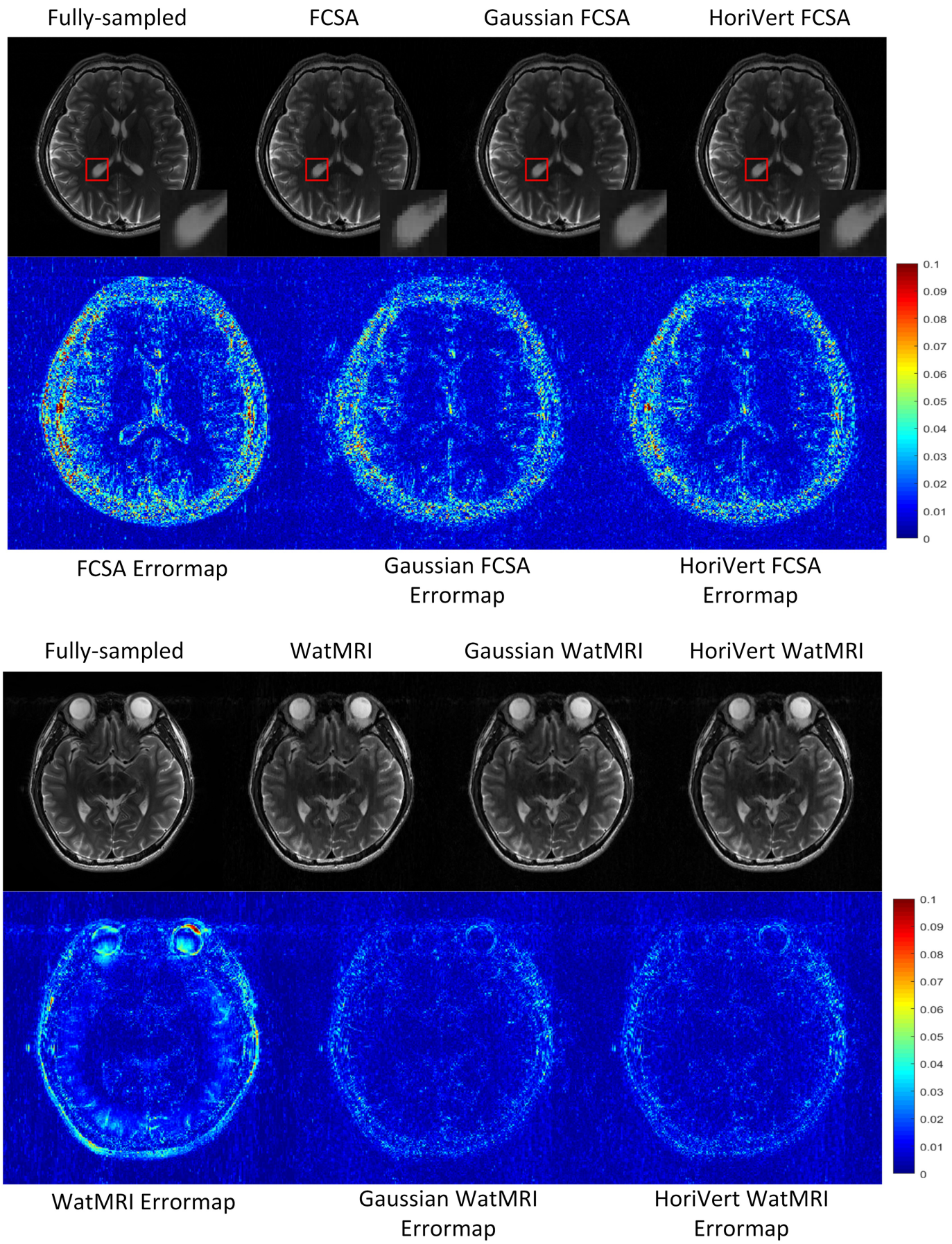

Fig. 11. The reconstruction results of FCSA and WatMRI using the 15% radial sampling mask on Gaussian and HoriVert subspace schemes and their corresponding error maps.

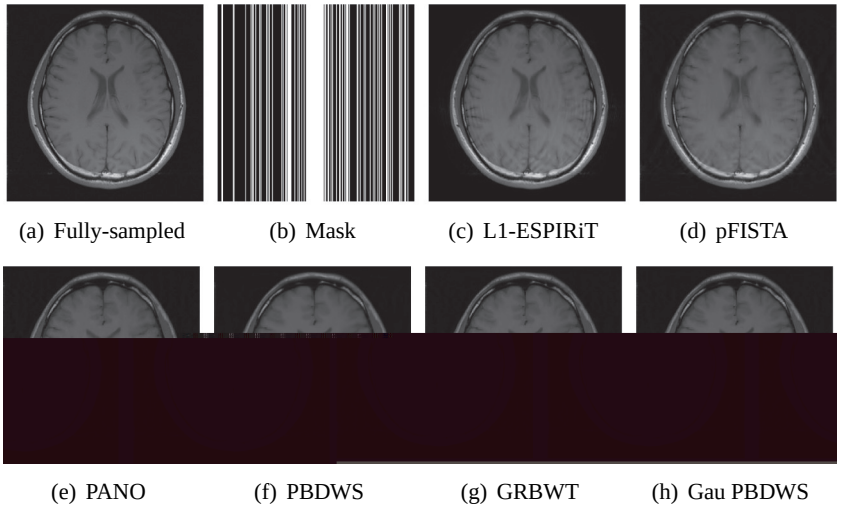

Fig. 12. Experiments conducted on T1wBrain data using various CS-MRI methods with 35% Cartesian under-sampling. We note that L1-ESPIRiT is a parallel imaging CS-MRI algorithm.

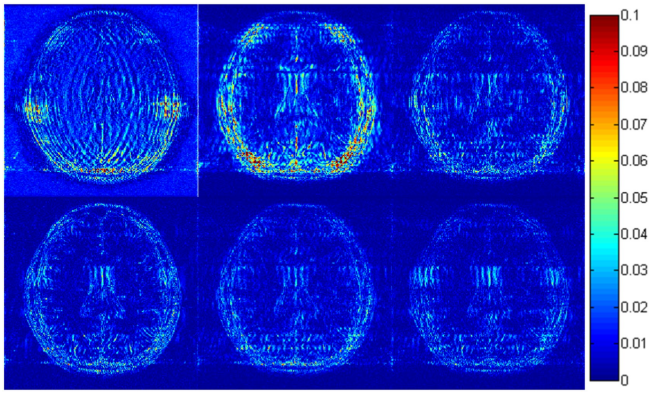

Fig. 13. The error residual images in Fig. 12. We note the proposed DAC framework applied to the PBDWS algorithm using Gaussian subspace decomposition achieves the minimum reconstruction error. The first row corresponds to Fig. 12c, d, e and the second row corresponds to Fig. 12f, g, h.

meters on the same magnitudes.

As for the parameter setting in subspace integration, we found that model performance was already good by setting all the subspace integration parameters the same. These parameter can also be estimated via the proposed scheme in Algorithm 1 using the augmented Lagrangian method. In this way, the strict equality of the subspace decomposition holds.

4.2. Discussion on noisy environments

During the acquisition of MRI measurements, the contamination brought by noise is inevitable. The SNR index for the high frequency subspace decreases because the noise is amplified. As discussed in Section 2, the magnitudes of the high frequency subspace MRI are small yet important, because it contains structural information and fine details. With an efficient CS-MRI algorithm, we can denoise the high frequency subspace MR images while retaining image structures because CS-MRI algorithms can benefit from high sparsity.

Table 2
The experiment on DAC version of FCSA using same parameter setting as direct FCSA.

	FCSA	Gaussian FCSA	HoriVert FCSA
PSNR (dB)	33.78	34.74	34.20
SSIM	0.914	0.922	0.915

We experimented with simulated noisy environments to evaluate the performance of the proposed DAC framework by adding the Gaussian noise into the under-sampled k-space. We conducted experiments on the 27^{th} slice of the T2wBrain image, where we used 25% 2D random mask for under-sampling. We added Gaussian random noise to the k-space with various standard deviations from 0.01 to 0.05 to evaluate its robustness to noise using both PBDWS methods. We show the performance curve for PSNR and SSIM with respect to different noise level in Fig. 15. The experiments show that the proposed DAC framework is robust to noise contamination in k-space. The proposed DAC framework also outperformed in SSIM, meaning the high frequency information still better reconstructed in the presence of noise, despite its larger relative magnitude in this region. The margin to which the DAC frameworks outperformed the regular counterparts increased as the noise level went up.

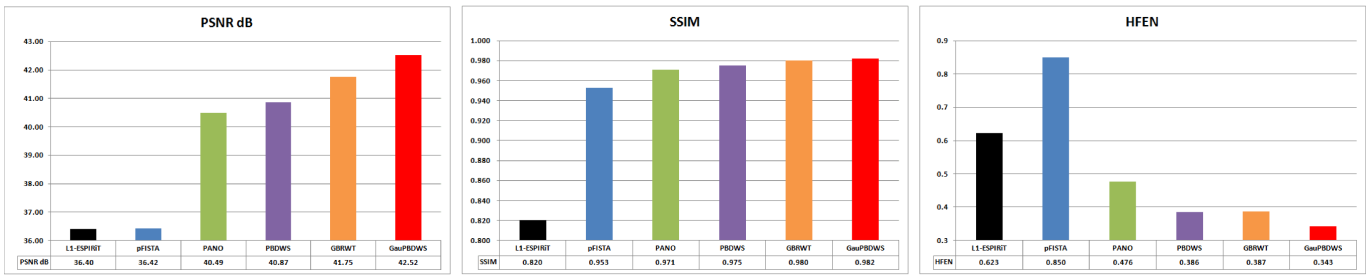

Fig. 14. The PSNR, SSIM and HFEN index for the experiments conducted on T1wBrain data with 35% Cartesian under-sampling.

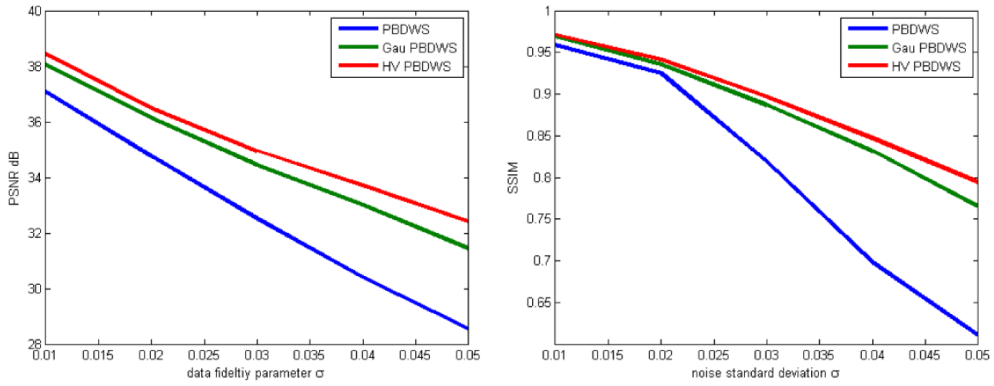

(a) PSNR (b) SSIM

Fig. 15. Experiments conducted on T2wBrain slice27 data using PBDWS and its DAC counterparts with 25% random under-sampling. Zero-mean Gaussian noise is added with standard deviation ranging from 0.01 to 0.05.

5. Conclusion

Based on the common observation that the energy and sparsity of k-space is non-uniformly distributed, we propose a divide-and-conquer framework for CS-MRI inversion. We first apply a series of linear filters to decompose the sub-sampled k-space measurements into separate frequency views called subspaces. For this, we use two filtering schemes called HoriVert decomposition and Gaussian decomposition based on the linear-vertical and Gaussian filters. We then reconstruct the corresponding MRI in each subspace independently using any off-the-shelf CS-MRI inversion algorithm. We obtain the final reconstructed MRI by integrating all the reconstructed subspace images using Tikhonov regularization.

The experimental results on simulated phantom data and acquired complex-valued T2wBrain and T1wBrain MRI data show that the proposed subspace method can improve the performance of existing state-of-the-art CS-MRI methods considerably. We also observe that the proposed method has potential for recovering finer high frequency details for diagnosis, which may improve the reliability and effectiveness of CS-MRI.

Acknowledgments

This work was supported in part by the National Natural Science Foundation of China under Grants 61571382,81671766,61571005, 81671674,61671309 andU160525 , in part by the Fundamental Research Funds for the Central Universities under Grants 20720160075 and20720180059 , in part by the CCF-Tencent open fund and, the Natural Science Foundation of Fujian Province of China (No .2017J01126). L. Sun conducted portions of this work at Columbia University under China Scholarship Council grant (No .201806310090).

References

[1] Candès E J, Romberg J, Tao T. Robust uncertainty principles: exact signal reconstruction from highly incomplete frequency information. IEEE Trans Inf Theory 2006;52(2):489–509.
[2] Donoho D L. Compressed sensing. IEEE Trans Inf Theory 2006;52(4):1289–306.
[3] Yang G, Yu S, Dong H, Slabaugh G, Dragotti P L, Ye X, et al. DAGAN: deep de-aliasing generative adversarial networks for fast compressed sensing MRI reconstruction. IEEE Trans Med Imaging 2018;37(6):1310–21.
[4] Lyu J, Nakarmi U, Liang D, Sheng J, Ying L. KerNL: kernel-based nonlinear approach to parallel MRI reconstruction. IEEE Trans Med Imaging 2019;38(1):312–21.
[5] Godino-Moya A, Royuela-del Val J, Usman M, Menchón-Lara R-M, Martín-Fernández M, Prieto C, et al. Space-time variant weighted regularization in compressed sensing cardiac cine MRI. Magn Reson Imaging 2019.
[6] Lustig M, Donoho D, Pauly J M. Sparse MRI: the application of compressed sensing for rapid MR imaging. Magn Reson Imaging 2007;58(6):1182–95.
[7] Patel V M, Maleh R, Gilbert A C, Chellappa R. Gradient-based image recovery methods from incomplete Fourier measurements. IEEE Trans Image Process 2012;21(1):94–105.
[8] Liu Q, Wang S, Ying L, Peng X, Zhu Y, Liang D. Adaptive dictionary learning in sparse gradient domain for image recovery. IEEE Trans Image Process 2013;22(12):4652–63.
[9] Qu X, Zhang W, Guo D, Cai C, Cai S, Chen Z. Iterative thresholding compressed sensing MRI based on contourlet transform. Inverse Prob Sci Eng 2010;18(6):737–58.
[10] Qu X, Guo D, Ning B, Hou Y, Lin Y, Cai S, et al. Undersampled MRI reconstruction with patch-based directional wavelets. Magn Reson Imaging 2012;30(7):964–77.
[11] Ning B, Qu X, Guo D, Hu C, Chen Z. Magnetic resonance image reconstruction using trained geometric directions in 2D redundant wavelets domain and non-convex optimization. Magn Reson Imaging 2013;31(9):1611–22.
[12] Lai Z, Qu X, Liu Y, Guo D, Ye J, Zhan Z, et al. Image reconstruction of compressed sensing MRI using graph-based redundant wavelet transform. Med Image Anal 2016;27:93–104.
[13] Ravishankar S, Bresler Y. MR image reconstruction from highly undersampled k-space data by dictionary learning. IEEE Trans Med Imaging 2011;30(5):1028–41.
[14] Huang Y, Paisley J, Lin Q, Ding X, Fu X, Zhang X-P. Bayesian nonparametric dictionary learning for compressed sensing MRI. IEEE Trans Image Process 2014;23(12):5007–19.
[15] Chen C, Huang J. The benefit of tree sparsity in accelerated MRI. Med Image Anal 2014;18(6):834–42.
[16] Huang J, Zhang S, Metaxas D. Efficient MR image reconstruction for compressed MR imaging. Med Image Anal 2011;15(5):670–9.
[17] Chen C, Li Y, Huang J. Forest sparsity for multi-channel compressive sensing. IEEE Trans Signal Process 2014;62(11):2803–13.
[18] Sendur L, Selesnick I W. Bivariate shrinkage functions for wavelet-based denoising exploiting interscale dependency. IEEE Trans Signal Process 2002;50(11):2744–56.
[19] Yang Y, Liu F, Xu W, Crozier S. Compressed sensing MRI via two-stage reconstruction. IEEE Trans Biomed Eng 2015;62(1):110–8.
[20] Peng X, Liang D. MR image reconstruction with convolutional characteristic constraint (CoCCo). IEEE Signal Process Lett 2015;22(8):1184–8.
[21] Sung K, Hargreaves B A. High-frequency subband compressed sensing MRI using quadruplet sampling. Magn Reson Med 2013;70(5):1306–18.
[22] Park S, Park J. Compressed sensing MRI exploiting complementary dual decomposition. Med Image Anal 2014;18(3):472–86.
[23] Gonzalez R C. Digital image processing. NY: Woods Interscience; 2001.
[24] Smith D, Welch E. Non-sparse phantom for compressed sensing MRI reconstruction. International Society for Magnetic Resonance in Medicine 19th Scientific Meeting-ISMRM. vol. 11. 2011. p. 2845.
[25] Qu X, Hou Y, Lam F, Guo D, Zhong J, Chen Z. Magnetic resonance image reconstruction from undersampled measurements using a patch-based nonlocal operator. Med Image Anal 2014;18(6):843–56.
[26] Uecker M, Lai P, Murphy M J, Virtue P, Elad M, Pauly J M, et al. ESPIRiT — an eigenvalue approach to autocalibrating parallel MRI: where SENSE meets GRAPPA. Magn Reson Med 2014;71(3):990–1001. https://doi.org/10.1002/mrm.24751.
[27] Liu Y, Zhan Z, Cai J-F, Guo D, Chen Z, Qu X. Projected iterative soft-thresholding algorithm for tight frames in compressed sensing magnetic resonance imaging. IEEE Trans Med Imaging 2016;35(9):2130–40.